INSTITUTE OF PHYSICS PUBLISHING JOURNAL OF OPTICS B: QUANTUM AND SEMICLASSICAL OPTICS

J. Opt. B: Quantum Semiclass. Opt. **4** (2002) S82–S89 PII: S1464-4266(02)30451-8

Orbital angular momentum of a high-order Bessel light beam

K Volke-Sepulveda[1], V Garcés-Chávez[2], S Chávez-Cerda[1], J Arlt[2] and K Dholakia[2,3]

[1] Instituto Nacional de Astrofisica, Optica y Electronica, Apdo. Postal 51/216, Puebla, Pue., México 72000

[2] School of Physics and Astronomy, University of St. Andrews, North Haugh, St. Andrews, Fife KY16 9SS, Scotland

E-mail: kd1@st-and.ac.uk

Received 2 November 2001, in final form 25 February 2002
Published 28 March 2002
Online at stacks.iop.org/JOptB/4/S82

Abstract

The orbital angular momentum density of Bessel beams is calculated explicitly within a rigorous vectorial treatment. This allows us to investigate some aspects that have not been analysed previously, such as the angular momentum content of azimuthally and radially polarized beams. Furthermore, we demonstrate experimentally the mechanical transfer of orbital angular momentum to trapped particles in optical tweezers using a high-order Bessel beam. We set transparent particles of known dimensions into rotation, where the sense of rotation can be reversed by changing the sign of the singularity. Quantitative results are obtained for rotation rates.

Keywords: Orbital angular momentum density, Bessel light beams, optical tweezers

M This article features online multimedia enhancements

1. Introduction

It is well established that electromagnetic radiation may carry spin angular momentum (SAM) due to circular polarization. Additionally a light beam may possess orbital angular momentum (OAM) due to its spatial phase distribution.

Whilst it is recognized that light beams with an azimuthal phase term of the form $\exp\{+il\varphi\}$ possess OAM this is not exclusive and other forms of light beams may possess orbital angular momentum [1]. Most attention in the literature regarding beams with helical wavefronts has been dedicated to Laguerre–Gaussian (LG) laser modes [2]. In 1992 the OAM for LG beams was calculated for the first time within the paraxial approximation for the cases of linear and circular polarization [3]. This has generated substantial theoretical and experimental activity in recent years.

However, there are important differences between LG beams and other rotating fields, such as high-order Bessel beams (BBs), that may lead to different potential applications. Bessel beams are solutions of the Helmholtz equation that are propagation invariant [4, 5]. These beams, also called 'non-diffracting' beams, have generated considerable interest in recent years. For instance, Arlt *et al* [6] have recently established a comparison between LG beams and BBs for cold atom guiding. They concluded that for focusing an atomic ensemble it is convenient to use LG modes with radial index $p = 0$, but for atom transport over extended distances BBs are extremely advantageous over LG beams due to their propagation invariant properties.

There is another motivation for analysing in detail the properties of BBs related with angular momentum. The Bessel functions are solutions of the exact Helmholtz equation but also of the paraxial wave equation. This may open the possibility of experimental studies in the paraxial and nonparaxial regimes. A vectorial analysis of angular momentum was done for nonparaxial beams with near-cylindrical symmetry and, although BBs were mentioned as a particular case, they were not analysed in detail [7].

Interest in the orbital angular momentum of light beams has initiated a number of experimental studies. It has been

[3] Author to whom correspondence should be addressed.

demonstrated that both OAM and SAM can be transferred to microparticles and cold atoms [8–10]. Further work has also shown the mechanical equivalence of spin and orbital angular momentum so that they can be added to give the total angular momentum in such systems [11, 12]. Recently, Allen and Padgett [13] suggested that, in an experiment, atoms may respond to the local value of angular momentum, which may not only be different in magnitude but may also have a different sign from that expected by the state of polarization of the beam. However, all experimental studies have exclusively concentrated on LG beams and have not explored the wider family of light beams or mode profiles that are also theoretically noted to possess orbital angular momentum.

In this paper, we calculate explicitly angular momentum density for BBs within a rigorous vectorial treatment in the nonparaxial regime. In the paraxial limit our results reproduce the well-known expressions for angular momentum that were originally derived for LG beams and later generalized to any paraxial beam with helical wavefronts [3]. Indeed, the angular momentum density of BBs is similar to that of multi-ringed LG beams, i.e. $p > 0$, which is not too surprising as BBs can be regarded as the limiting case for LG beams with increasing radial mode index p. However, when the nonparaxiality is relevant, the local angular momentum shows significant variations. Furthermore, high-order Bessel beams are easier to generate experimentally than multi-ringed LG beams. Here we demonstrate experimentally, for the first time to our knowledge, the mechanical transfer of OAM to trapped particles in optical tweezers using a high-order Bessel beam. We set transparent particles of known dimensions into rotation. Quantitative results are obtained for the rotation rate which has a linear dependence on the orbital angular momentum content of the light beam.

2. Different states of polarization for BBs

For a linearly polarized electromagnetic field a scalar treatment is adequate under certain circumstances [14]. However, in a rigorous manner, the electromagnetic field behaviour is determined by the vectorial wave equation.

In this analysis we assume monochromatic fields, as any arbitrary time dependence can be expanded in terms of harmonic functions. In this case, the vectorial wave equation for an homogeneous and isotropic medium reduces to the vectorial Helmholtz equation, that is

$$\nabla^2 \boldsymbol{C}(\boldsymbol{r}) + k^2 \boldsymbol{C}(\boldsymbol{r}) = 0 \tag{1}$$

where the vector $\boldsymbol{C}(\boldsymbol{r})$ can represent either electric or magnetic induction field, as well as vector potential, and $k = \omega/c$ is the wavenumber.

The most general solution to equation (1) is given by [15]

$$\boldsymbol{C}(\boldsymbol{r}) = \sum_l (a_l \boldsymbol{M}_l(\boldsymbol{r}) + b_l \boldsymbol{N}_l(\boldsymbol{r}) + c_l \boldsymbol{L}_l(\boldsymbol{r})) \tag{2}$$

where

$$\boldsymbol{M}_l(\boldsymbol{r}) = \nabla \times \hat{\boldsymbol{a}} \psi_l(\boldsymbol{r}) \tag{3}$$

$$\boldsymbol{N}_l(\boldsymbol{r}) = \frac{1}{k} \nabla \times \boldsymbol{M}_l(\boldsymbol{r}) \tag{4}$$

$$\boldsymbol{L}_l(\boldsymbol{r}) = \nabla \psi_l(\boldsymbol{r}) \tag{5}$$

with $\hat{\boldsymbol{a}}$ being an arbitrary unit vector and $\psi_l(\boldsymbol{r})$ being a member of a complete set of solutions of the scalar Helmholtz equation. The coefficients a_l, b_l and c_l are determined by the boundary conditions or by the symmetry of the specific situation.

It can be easily verified using Maxwell equations that, if the vector potential $\boldsymbol{A}$ is given by a general expansion of the form (2), the fields $\boldsymbol{E}$ and $\boldsymbol{H}$ will be given just in terms of the vectors $\boldsymbol{M}_l$ and $\boldsymbol{N}_l$. The vector $\boldsymbol{L}_l$ will not appear in the expression for $\boldsymbol{B}$, as $\boldsymbol{B} = \nabla \times \boldsymbol{A}$. This is consistent with the fact that both $\boldsymbol{M}_l$ and $\boldsymbol{N}_l$ are solenoidal and each is proportional to the curl of the other, like the electric and magnetic fields. Then, we can write $\boldsymbol{E}$ as [15]

$$\boldsymbol{E}(\boldsymbol{r}) = \sum_l (a_l \boldsymbol{M}_l(\boldsymbol{r}) + b_l \boldsymbol{N}_l(\boldsymbol{r})). \tag{6}$$

It is important to note that expression (6) is completely general since it does not depend on the coordinate system under consideration.

In particular, for the case of circular cylindrical coordinates, the solution to the scalar Helmholtz equation is

$$\psi_l(\rho, \varphi, z) = J_l(k_t \rho) \exp(\mathrm{i} l \varphi + \mathrm{i} k_z z) \tag{7}$$

where J_l is the lth-order Bessel function. Equation (7) is precisely what we can identify as the amplitude distribution of BBs, where l represents the azimuthal index, and k_t and k_z are the transversal and longitudinal components of the wave vector.

By taking the arbitrary constant vector $\hat{\boldsymbol{a}}$ as the unit vector in the z-direction, $\boldsymbol{u}_z$, and by using equation (7) in equations (3) and (4), after simple calculations it is obtained that

$$\boldsymbol{M}_{\boldsymbol{u}_z l} = \frac{k_t}{2} \{\mathrm{i}(J_{l-1} + J_{l+1}) \boldsymbol{u}_\rho - (J_{l-1} - J_{l+1}) \boldsymbol{u}_\varphi\} \mathrm{e}^{\mathrm{i} k_z z + \mathrm{i} l \varphi} \tag{8}$$

$$\boldsymbol{N}_{\boldsymbol{u}_z l} = \frac{k_t}{2k} [\mathrm{i} k_z (J_{l-1} - J_{l+1}) \boldsymbol{u}_\rho - k_z (J_{l-1} + J_{l+1}) \boldsymbol{u}_\varphi + 2 k_t J_l \boldsymbol{u}_z] \mathrm{e}^{\mathrm{i} k_z z + \mathrm{i} l \varphi} \tag{9}$$

where the arguments of the functions were omitted for brevity. These equations lead to the cases of radially and azimuthally polarized beams, as well as to linear ($\mathcal{P}$), right-circular ($\mathcal{R}$) and left-circular ($\mathcal{L}$) polarization states.

The electric field vector for azimuthal polarization is obtained by using equations (8) and (9) in expression (6) and setting $a_l = \delta_{0l}(2E_0/k_t)$; $b_l = 0$, which gives

$$\boldsymbol{E}_a(r) = E_0 J_1(k_t \rho) \mathrm{e}^{\mathrm{i} k_z z} \boldsymbol{u}_\varphi \tag{10}$$

where E_0 is a constant proportional to the square root of the incident power and with electric field units.

Azimuthal polarization can be interpreted as the transversal electric mode (TE) for BBs, as it is the only case in which the electric vector has no component in the z-direction. This result will be more evident from the general expression for the electric field of $\mathcal{P}$, $\mathcal{R}$ and $\mathcal{L}$ states, equation (12), where it can be seen that in these cases there is always a longitudinal component.

For the radial polarization state, which corresponds to a transversal magnetic mode (TM), setting the coefficients $a_l = 0$ and $b_l = \delta_{0l}(2\mathrm{i}E_0 k/k_z k_t)$ in (6) and from equations (8) and (9), the electric field vector is

$$\boldsymbol{E}_r(r) = E_0 \left[J_1(k_t \rho) \boldsymbol{u}_\rho + 2\mathrm{i} \left(\frac{k_t}{k_z} \right) J_0(k_t \rho) \boldsymbol{u}_z \right] \mathrm{e}^{\mathrm{i} k_z z}. \tag{11}$$

On the other hand, to construct the general expressions for $\mathcal{R}$ and $\mathcal{L}$ states by means of equations (8) and (9), it is necessary to set $b_l = (k/k_z)a_l$ and $b_l = -(k/k_z)a_l$, respectively, in equation (6). Orthogonal $\mathcal{P}$ states can be constructed as a superposition of $\mathcal{R}$ and $\mathcal{L}$ states.

Once we obtain the two orthogonal $\mathcal{P}$ states we are in a position to write the most general expression for the field as

$$\boldsymbol{E}(\boldsymbol{r}) = E_0 \mathrm{e}^{\mathrm{i}(k_z z + l\varphi)} \left\{ [\alpha \boldsymbol{u}_x + \beta \boldsymbol{u}_y] J_l + \frac{\mathrm{i}}{2}\left(\frac{k_t}{k_z}\right) \times [(\alpha + \mathrm{i}\beta)\mathrm{e}^{-\mathrm{i}\varphi} J_{l-1} - (\alpha - \mathrm{i}\beta)\mathrm{e}^{\mathrm{i}\varphi} J_{l+1}]\boldsymbol{u}_z \right\} \tag{12}$$

where α is the x-component and β is the y-component of the corresponding Jones vector for the given polarization state. In particular, for linear polarization both of these parameters are real, while for right- and left-circular polarization they satisfy $\beta = \mathrm{i}\alpha$ and $\beta = -\mathrm{i}\alpha$, respectively. Equation (12) agrees with the corresponding expression presented in [7] that was obtained in a different way. However, having the fields expressed in terms of powers of (k_t/k_z) allows us to make an analysis in the limit of the paraxial approximation when $k_t \ll k_z$ as well as in the nonparaxial regime for which this inequality is not satisfied.

It should be noted that for an $\mathcal{R}$ state, $\beta = \mathrm{i}\alpha$, the first term of the z-component in (12) vanishes, and the transversal vectors $(\boldsymbol{u}_x + \mathrm{i}\boldsymbol{u}_y)$ can be written in polar coordinates giving $(\boldsymbol{u}_\rho + \mathrm{i}\boldsymbol{u}_\varphi)\mathrm{e}^{\mathrm{i}\varphi}$, so the azimuthal phase dependence of electric vector is in this case $\exp\{\mathrm{i}(l+1)\varphi\}$ instead of $\exp\{\mathrm{i}l\varphi\}$. Similarly, for the $\mathcal{L}$ state we find that the azimuthal dependence is now of the form $\exp\{\mathrm{i}(l-1)\varphi\}$. Moreover, this is not only valid for BBs, but for any field with circular polarization, since even if it does not have another kind of azimuthal dependence, it will possess a term of the form $\exp\{\pm\mathrm{i}\varphi\}$ due to the polarization when analysed in polar coordinates.

3. Poynting vector and angular momentum density

It is well known that the energy flux of the radiation field is given by the Poynting vector $\boldsymbol{S}$, which in free space is also proportional to the linear momentum density $\boldsymbol{g} = \boldsymbol{S}/c^2$. And the angular momentum density can be expressed as $\boldsymbol{j} = \boldsymbol{r} \times \boldsymbol{S}/c^2$ [16].

We can use the expressions for the electric field $\boldsymbol{E}$ which we have obtained in the previous section to calculate the real part of the time-averaged Poynting vector, given by $\langle \boldsymbol{S} \rangle = (1)/(4\mathrm{i}\omega\mu)\{\boldsymbol{E} \times \nabla \times \boldsymbol{E}^* + \boldsymbol{E}^* \times \nabla \times \boldsymbol{E}\}$. The total linear and angular momenta can be obtained by integrating the corresponding momentum densities over the whole space.

3.1. Azimuthal and radial polarization states

For pure azimuthal and radial polarizations of BBs we find, using either equation (10) or (11), identical results for the Poynting vector

$$\langle \boldsymbol{S} \rangle = \frac{|E_0|^2 k_z}{2\omega\mu_0} [J_1(k_t\rho)]^2 \boldsymbol{u}_z \tag{13}$$

which means that for these polarizations the energy flux and the linear momentum of the fields are only in the longitudinal direction.

On the other hand, for the real part of the time-averaged angular momentum density we have

$$\langle \boldsymbol{j} \rangle = -\frac{|E_0|^2 k_z}{2\omega\mu_0 c^2} \rho [J_1(k_t\rho)]^2 \boldsymbol{u}_\varphi. \tag{14}$$

When an integration is realized over the whole space in order to calculate the total angular momentum, the azimuthal components of $\langle \boldsymbol{j} \rangle$ will cancel out by symmetry, and this is also true for a finite integration region provided that it be centre symmetric. In consequence, we can conclude that BBs with pure azimuthal or pure radial polarization do not carry angular momentum. This is not surprising since these modes do not possess an azimuthal phase dependence, implying that they are not rotating waves.

To understand the physical significance of this fact, we rewrite equations (10) and (11) in terms of the rectangular unit vectors $\boldsymbol{u}_x$ and $\boldsymbol{u}_y$, using the relations $\boldsymbol{u}_\rho = \boldsymbol{u}_x \cos\varphi + \boldsymbol{u}_y \sin\varphi$ and $\boldsymbol{u}_\varphi = -\boldsymbol{u}_x \sin\varphi + \boldsymbol{u}_y \cos\varphi$, and we obtain

$$\boldsymbol{E}_a(\boldsymbol{r}) = E_0 \mathrm{e}^{\mathrm{i}(k_z z + \pi/2)} \frac{J_1(k_t\rho)}{2} [\mathrm{e}^{\mathrm{i}\varphi}(\boldsymbol{u}_x - \mathrm{i}\boldsymbol{u}_y) - \mathrm{e}^{-\mathrm{i}\varphi}(\boldsymbol{u}_x + \mathrm{i}\boldsymbol{u}_y)] \tag{15}$$

$$\boldsymbol{E}_r(\boldsymbol{r}) = E_0 \mathrm{e}^{\mathrm{i}k_z z} \left\{ \frac{J_1(k_t\rho)}{2} [\mathrm{e}^{\mathrm{i}\varphi}(\boldsymbol{u}_x - \mathrm{i}\boldsymbol{u}_y) + \mathrm{e}^{-\mathrm{i}\varphi}(\boldsymbol{u}_x + \mathrm{i}\boldsymbol{u}_y)] + 2\mathrm{i}\left(\frac{k_t}{k_z}\right) J_0(k_t\rho)\boldsymbol{u}_z \right\}. \tag{16}$$

These expressions reveal that pure azimuthal and radial polarized fields are appropriate superpositions of two beams: one with $l = 1$ and spin $= -1$ (left-circularly polarized), and the other with $l = -1$ and spin $= 1$ (right-circularly polarized). Then the total spin and the total orbital angular momenta of each superposition are zero. This explains, from a physical point of view, why pure azimuthally and radially polarized beams do not carry angular momentum. Additionally, this also suggests an experimental way to generate beams with these polarization states.

3.2. Linear and circular polarization states

For $\mathcal{P}$, $\mathcal{R}$ and $\mathcal{L}$ states, the general expression of the Poynting vector obtained from equation (12) is given by

$$\langle \boldsymbol{S} \rangle = \frac{|E_0|^2}{4\omega\mu_0} \left\{ \left[\frac{2l}{\rho} J_l^2 - \sigma \frac{\mathrm{d}}{\mathrm{d}\rho} J_l^2 \right] \boldsymbol{u}_\varphi + 2k_z \left[J_l^2 + \frac{1}{4}\left(\frac{k_t}{k_z}\right)^2 (2J_l^2 + J_l(J_{l+2} - J_{l-2}) \times \{(|\alpha|^2 - |\beta|^2)\cos 2\varphi + 2\mathrm{Re}\{\alpha^*\beta\}\sin 2\varphi\}) \right] \boldsymbol{u}_z \right\} + \boldsymbol{U} \tag{17}$$

where $\boldsymbol{U}$ is a transverse vectorial function of second and third order in k_t/k_z. The explicit form of $\boldsymbol{U}$ is rather large and to avoid confusion at this stage it is given in the appendix. We assume $(|\alpha|^2 + |\beta|^2) = 1$ and $\sigma = \mathrm{i}(\alpha\beta^* - \alpha^*\beta)$, which is the same convention as that used in [7]. It can be easily verified that $\sigma = 0, +1, -1$, for $\mathcal{P}$, $\mathcal{R}$ and $\mathcal{L}$ states, respectively.

For the angular momentum density we have

$$\langle \boldsymbol{j} \rangle = \frac{|E_0|^2}{4\omega\mu_0 c^2} \left\{ -z \left[\frac{2l}{\rho} J_l^2 - \sigma \frac{\mathrm{d}}{\mathrm{d}\rho} J_l^2 \right] \boldsymbol{u}_\rho - 2\rho k_z \right.$$

$$\times\left[J_l^2+\frac{1}{4}\left(\frac{k_t}{k_z}\right)^2\{2J_l^2+J_l(J_{l+2}-J_{l-2})[(|\alpha|^2-|\beta|^2)\right.$$
$$\times\cos 2\varphi+2\mathrm{Re}\,\{\alpha^*\beta\}\sin 2\varphi]\}\Big]\boldsymbol{u}_\varphi$$
$$\left.+\rho\left[\frac{2l}{\rho}J_l^2-\sigma\frac{\mathrm{d}}{\mathrm{d}\rho}J_l^2\right]\boldsymbol{u}_z\right\}+(\boldsymbol{r}\times\boldsymbol{U}). \quad (18)$$

As in the radial and azimuthal polarization cases, if an integration over the whole space is realized to calculate the total angular momentum, the radial and azimuthal components of the angular momentum density vanish, so that the total angular momentum is just directed along the propagation axis for $\mathcal{P}$, $\mathcal{R}$ and $\mathcal{L}$ states.

From equations (18) and (23), given in the appendix, it is possible to obtain the z-component of the angular momentum density corresponding to the Helmholtz equation, namely

$$j_z=\frac{|E_0|^2\epsilon_0}{2\omega}\left\{\left[lJ_l^2-\frac{1}{2}\sigma\rho\frac{\mathrm{d}}{\mathrm{d}\rho}J_l^2\right]+\left(\frac{k_t}{k_z}\right)^2\right.$$
$$\times[2lJ_l^2(|\alpha\sin\varphi-\beta\cos\varphi|^2)]+\frac{1}{2}\left(\frac{k_t}{k_z}\right)^3k_z\rho$$
$$\times[\{(1-\sigma)J_{l-1}J_{l-2}+(1+\sigma)J_{l+1}J_{l+2}-\sigma J_l(J_{l-1}-J_{l+1})$$
$$-[(|\alpha|^2-|\beta|^2)\cos 2\varphi+2\mathrm{Re}\,(\alpha^*\beta)\sin 2\varphi]$$
$$\left.\times(J_{l-2}J_{l+1}+J_{l+2}J_{l-1})]\right\}. \quad (19)$$

On the other hand, in the paraxial limit, for any electromagnetic field ψ with an azimuthal dependence of the form $\exp(\mathrm{i}l\varphi)$, like a BB when $k_t \ll k_z$ or LG beams, the z-component of the angular momentum density is [13]

$$j_z=\frac{|E_0|^2\epsilon_0}{2}\left\{\frac{l}{\omega}|\psi(\boldsymbol{r})|^2-\frac{\sigma\rho}{2\omega}\frac{\partial|\psi(\boldsymbol{r})|^2}{\partial\rho}\right\}. \quad (20)$$

The extra terms in equation (18) constitute an important difference of the angular momentum density of nonparaxial BBs with respect to that of paraxial beams. To appreciate the importance of this fact, we can consider an experimental situation for atom confinement with a conical mirror whose vertex angle is such that the ratio of the wave vector components of the resulting BB is not negligible. For instance, in figure 1(a) we show the spatial distribution of the z-component of the angular momentum density for a BB with $l=3$ and $k_t/k_z=0.7$, for a linearly polarized field, with the polarization plane inclined 45° with respect to the horizontal plane. We also show the distribution for (b) a paraxial BB with $k_t/k_z=0.05$, (c) an LG beam with $p=6$, and (d) an LG beam with $p=0$; in all the cases $l=3$. In figure 2 we show the corresponding pictures but now for right-handed circularly polarized fields. From these figures we remark on the fact that for the linearly polarized nonparaxial BB the angular momentum density distribution is not radially symmetric. This is also clear by analysing equation (19), since for circular polarization we have $|\alpha\sin\varphi-\beta\cos\varphi|^2=1/2$, and all the other terms depending on the azimuthal angle vanish. Also, for paraxial beams, equation (20) does not depend on the azimuthal coordinate at all. Therefore, the azimuthal dependence is relevant in the case of nonparaxial linearly polarized BBs, giving rise to an asymmetrical distribution of angular momentum density. It is worth noting that the asymmetry arises in the direction of the polarization plane. These type of asymmetries have been previously observed in connection with vectorial beams [18]. The angular momentum properties of nonparaxial BBs open the possibility of new experimental studies, though we note that high nonparaxial limits are difficult to achieve with refractive axicons and telescopes.

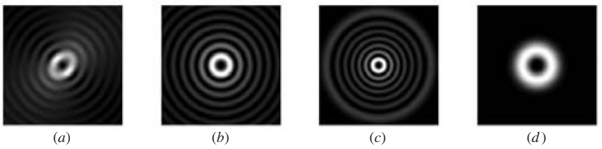

Figure 1. Longitudinal component of the angular momentum density of a linear polarization state for: (a) a nonparaxial BB with $l=3$ and $k_t/k_z=0.6$; (b) a paraxial BB with $l=3$ and $k_t/k_z=0.01$; (c) an LG beam with $l=3$ and $p=6$; (d) an LG beam with $l=3$ and $p=0$.

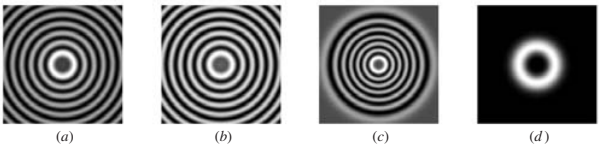

Figure 2. Longitudinal component of the angular momentum density of a right-circular polarization state for: (a) a nonparaxial BB with $l=3$ and $k_t/k_z=0.6$; (b) a paraxial BB with $l=3$ and $k_t/k_z=0.01$; (c) an LG beam with $l=3$ and $p=6$; (d) an LG beam with $l=3$ and $p=0$.

Later, we experimentally study the OAM for a paraxial BB, so that we restrict the following analysis to this regime. In figure 3 we show the intensity profile of the BB along with the z-component of the paraxial angular momentum density for $\mathcal{P}$, $\mathcal{R}$ and $\mathcal{L}$ states for some values of l. For comparison, in figure 4 analogous plots for LG beams for different values of l and p are shown. It can be seen from the figures that for circular polarization states the angular momentum density changes not only in magnitude but also in sign over the beam profile for all cases. This fact was mentioned in [13], nevertheless from the graphical analysis we can make an important remark. The shifting of the AM density maxima with respect to those of the intensity distribution, where particles could be trapped, might cause an additional torque. Also, notice that in the case of multi-ringed beams, BBs and LG beams with $p \geqslant 1$, the sign variations are more considerable than for a single-ring beam. However, approximations to BBs are easier to generate experimentally (see section 4) than multi-ringed LG beams, which require more specialized holograms or a cylindrical lens mode convertor.

So far we have considered a purely classical treatment. From a quantum mechanics perspective, it was demonstrated in [3] that the total angular momentum per photon for paraxial LG beams is given by $(l+\sigma)\hbar$. Furthermore, in [7] it has been recognized that this result has a general validity, within the paraxial approximation, for all kinds of beams possessing an azimuthal phase term of the form $\exp\{\pm\mathrm{i}l\phi\}$.

From an experimental point of view, the mechanism by which the transfer of angular momentum from radiation to matter takes place strongly determines its behaviour. For instance, if the mechanism is preferably absorption, the orbital

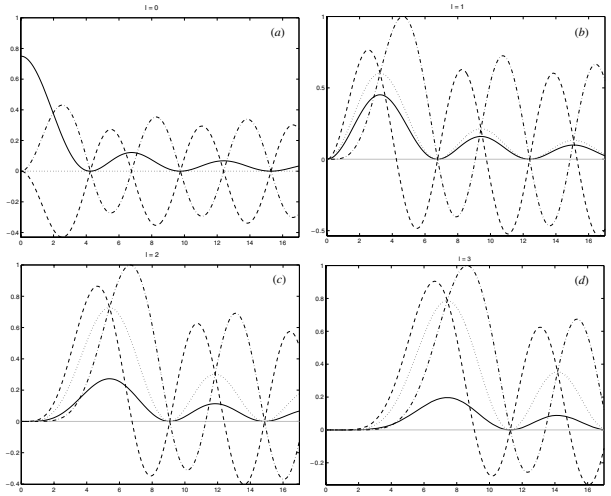

Figure 3. Comparison between the intensity distribution (solid curve) and the z-components of the angular momentum density for BBs with different azimuthal indices, for $\mathcal{P}$-state (dotted curve), $\mathcal{R}$-state (dash–dot curve) and $\mathcal{L}$-state (dashed curve). All the curves are normalized, the radius is given in micrometres, for $\theta = \tan^{-1}(k_t/k_z) = 5.5^\circ$ and $\lambda = 1064$ nm. The mode indices are $(a)\ l = 1$, $(b)\ l = 2$, $(c)\ l = 3$, $(d)\ l = 4$.

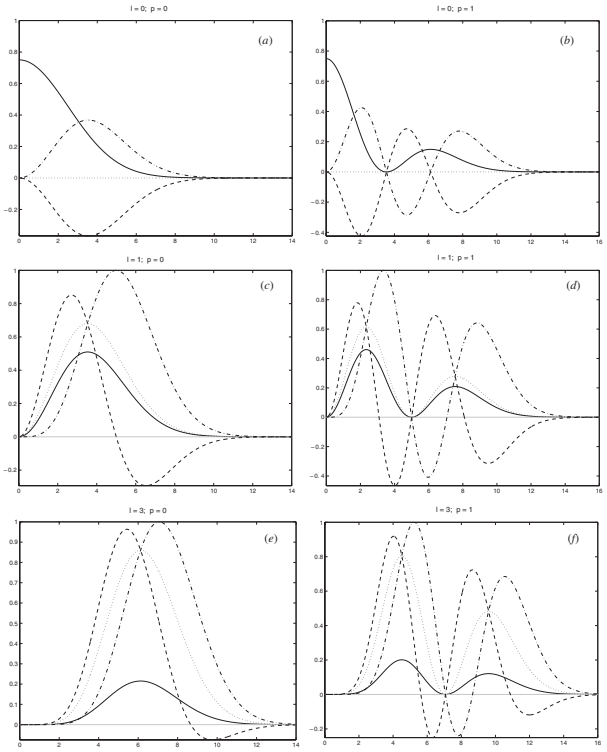

Figure 4. Comparison between the intensity distribution (solid curve) and the z-components of the angular momentum density for LG beams with different azimuthal and radial indices, for $\mathcal{P}$-state (dotted curve), $\mathcal{R}$-state (dash–dot curve) and $\mathcal{L}$-state (dashed curve). All the curves are normalized, the radius is given in micrometres, the beam waist was taken as 10 μm and $\lambda = 1064$ nm. The mode indices are $(a)\ l = 0$, $(b)\ l = 0$, $p = 1$, $(c)\ l = 1$, $p = 0$, $(d)\ l = 1$, $p = 1$, $(e)\ l = 3$, $p = 0$, $(f)\ l = 3$, $p = 1$.

and spin angular momenta appear to play equivalent roles in interaction with microparticles, so they can be added or subtracted to give the total angular momentum as in quantum mechanics [11, 12]. On the other hand, recent experiments suggest that, if scattering is the predominant mechanism of transfer, the effects produced by orbital and spin angular momenta can be decoupled, and only the effects of the OAM can be observed [9].

The different behaviour produced by OAM and SAM for various transfer mechanisms can be studied for a particle trapped in different rings within the BB. In particular, in the following section we present the first experimental confirmation of the orbital angular momentum content of a BB.

4. Experiment

4.1. Experimental set-up

To study the transfer of OAM from high-order BBs to particles we used an optical tweezers system similar to that described in [19]. The experimental set-up is shown in figure 5. Firstly, we expanded a linearly polarized Gaussian output beam of a cw Nd:YAG laser (1 W@1064 nm) to illuminate a computer-generated hologram [20]. This blazed phase hologram diffracted about 80% of the incident light into a first-order beam with helical wavefronts, giving a close approximation to an LG beam in the far field. This beam illuminated an axicon having an opening angle γ of 1°, thus generating an approximation to a higher-order BB [21]. A telescope ($\times 1/20$) was used to reduce the radius of the inner ring of the BB such that it was of a similar size as the trapped particles. The telescoping also resulted in a reduced propagation distance of the BB and increased its intensity. For a beam of azimuthal mode index $l = 3$ the inner ring of the imaged BB had a peak radius of about 3.8 μm and propagated for approximately $z_{max} = 1$ mm. This beam was directed downwards onto the sample mounted on an x–y–z translation stage. A microscope objective ($\times 60$) and CCD camera were placed below the sample for observation of the particles.

The propagation distance of our experimental approximation to a higher-order BB is fairly short and the peak intensity of the beam varies along this propagation distance [22]. Therefore the positioning of the sample cell along the propagation (z) direction is quite important. The sample should be located in the plane with the highest peak intensity in the inner ring. Experimentally this was achieved by placing the sample stage in the z-position where the transverse trapping of particles was strongest. The maximum laser power in the sample plane was about 600 mW. As all the rings of a BB contain a similar amount of its total power this corresponds to only about 15 mW in each of the 40 rings of our experimental BB.

We used two different holograms to generate a helical beam with azimuthal mode index $l = 2$ and 3, respectively. The alignment of the whole optical system was critical, as even slight astigmatism led to a break-up of the vortices and loss of the symmetrical beam profile. The quality of the BB is very important because any intensity variation around the central ring hinders the continuous rotation of trapped particles. For optimal alignment we found an azimuthal intensity variation of about 5% along the inner ring of the higher-order BB for both $l = 2$ and 3. This residual variation was mainly due to azimuthal intensity variations in the holographically generated

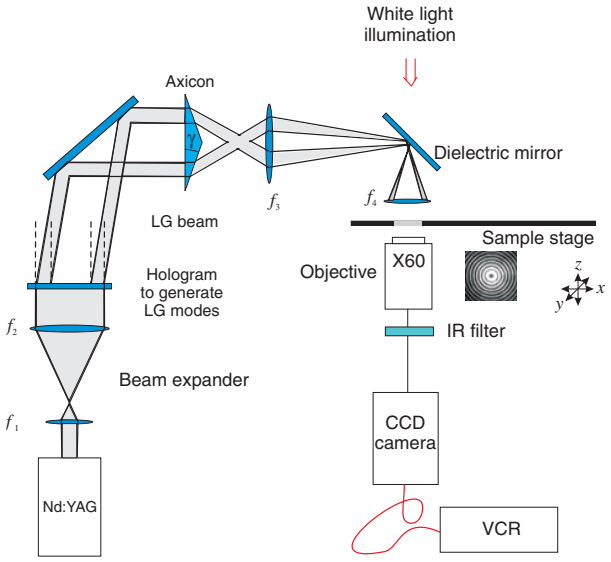

Figure 5. Experimental set-up for the transfer of OAM to spheres. Lenses $f_1 = 50$ mm and $f_2 = 250$ mm expand the beam to illuminate the hologram. The axicon is illuminated with the first-order diffracted beam from the hologram. Lenses $f_3 = 500$ mm and $f_4 = 25$ mm reduce the $l = 2$ Bessel light beam to one with a radius of the inner ring of 2.9 μm.

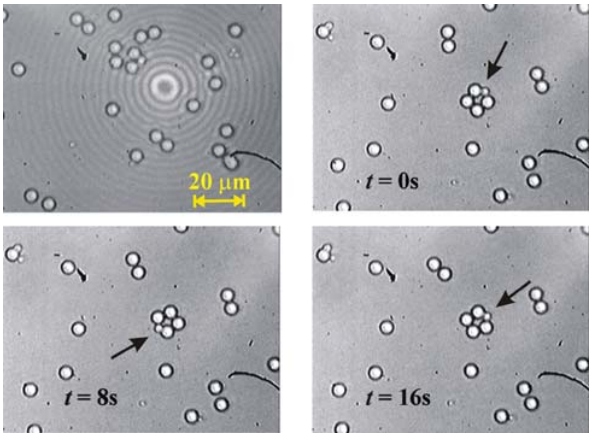

Figure 6. The first frame shows the transverse beam profile of the third-order Bessel light beam in the sample plane. The three successive frames show four 5 μm and one 1 μm spheres trapped in the inner ring of the beam. They continuously rotate around the circumference of the inner ring with a rotation rate of about 60 mHz (16 s per revolution). A MPEG movie of this figure is available from stacks.iop.org/JOptB/4/S82.

LG beam. As the alignment of the optical system for an $l = 2$ BB was less critical, the majority of the experimental results presented here were actually obtained with this l.

4.2. Results and discussion

We used different samples of transparent 1, 3 and 5 μm diameter silica spheres suspended in water. A small amount of detergent was added to the water to increase the mobility of the particles. In our initial experiments we used a BB with azimuthal mode index $l = 3$. The optical gradient force which acts on the transparent spheres results in a force directed towards the local intensity maximum [23]. In the case of the higher-order BB this means that the spheres were attracted to the annular regions of high laser intensity. The particles were confined to one of the rings and could be manipulated in the transverse dimensions similar to standard optical tweezers by either moving the sample stage or the final lens of the BB telescope.

By moving the sample stage we loaded several spheres into the inner ring until its whole circumference was filled with particles. This ring of spheres was found to rotate smoothly along the circumference of the inner ring (figure 6). Repeating the experiment with different groups of particles showed that the rotation was very reproducible. The rotation was always in anticlockwise sense and we observed consistent rotation periods of tens of seconds. We believe that this rotation arises from the azimuthal component of the Bessel beams momentum density, i.e. from a transfer of the beam's orbital angular momentum to the trapped group of particles.

Together with a very recent experiment by O'Neil *et al* [24] this is the first observation of orbital angular momentum transfer from a laser beam to transparent particles. Previous experiments relied either on absorption [8, 12] or used the scattering of metallic particles [9]. For transparent particles the orbital angular momentum is also transferred by scattering/reflection of the incident light beam as in the case of metallic particles. However, the scattering for transparent particles is low and therefore only a small fraction of the beam's orbital angular momentum is transferred to the particle. But as they are trapped in the high intensity region the transfer is sufficient to set them into rotation.

As the particles that we used were almost perfectly spherical the observed rotation cannot be due to unbalanced scattering of asymmetric particles. Furthermore, as the beam is directed downwards through the sample stage, the scattering force is predominantly downward and the torque produced by this scattering force would therefore be almost perpendicular to the beam axis.

We also directly determined the handedness of the beam as it passes through the sample plane by looking at the asymmetric diffraction on a knife edge (for details see [25]). We found that the Poynting vector and thus the orbital angular momentum follow a left-handed screw which is consistent with the measured sense of particle rotation (anticlockwise direction). Furthermore, we reversed the handedness of the higher-order BB by inserting a Dove prism and found that the sense of rotation of the trapped particles changes from anticlockwise to clockwise.

If the circumference of the inner ring is not filled completely with particles the rotation becomes more uneven. When loading the ring with particles we observed that even the first sphere preferentially starts moving along the ring in anticlockwise direction in agreement with the handedness of the beam's orbital angular momentum. However, we were not able to observe a continuous rotation of a single particle. We believe that this was due to the residual intensity variations along the inner ring of our experimental approximation to a Bessel beam. This gave rise to an azimuthal component of the gradient force. Single particles started to move along the ring, but only until they encountered an intensity hot-spot. There they got trapped as the torque transferred from the BB was not enough to overcome the azimuthal gradient force.

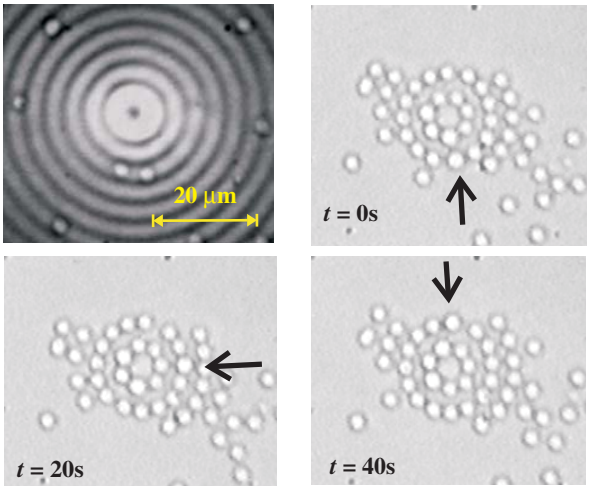

Figure 7. The first frame shows the second-order BB in the sample plane. Three successive frames show seven and fifteen 3 μm spheres trapped in the inner and second ring of this beam, respectively. Both rotate in the anticlockwise direction. The arrow tracks the motion of one sphere in the second ring. A MPEG movie of this figure is available from stacks.iop.org/JOptB/4/S82.

By carefully measuring the beam profile we verified that the positions in which the single spheres got stuck corresponded to local intensity maxima. As we increased the number of particles trapped in the inner ring they started to bunch up and eventually pushed each other through the intensity hot-spots. The group of particles then rotated continuously around the circumference. For low particle numbers this rotation was not very uniform, but if the circumference of the inner ring was filled almost completely a smooth rotation was observed. We believe that it should also be possible to rotate just a single sphere by increasing the amount of orbital angular momentum transferred to the particle. This could be achieved by increasing the laser power, by increasing the charge l of the BB (or by using a more efficient transfer mechanism such as absorption rather than scattering). Alternatively, improving the azimuthal uniformity of our experimental BB, for example by use of a cavity to clean up the holographically generated LG beam, would also make it possible to rotate single particles.

Furthermore, we have observed the rotation of spheres along the second inner ring of the $l = 2$ BB (figure 7). The particles rotate in the same sense but even more slowly than in the inner ring, typically with about a sixth of the rotation rate. This is to be expected as the increased radius of the particle trajectories leads to a decrease in particle velocity for a given angular momentum transfer.

As the rotation was very reproducible if a ring was filled completely with particles it was furthermore possible to study rotation rates. Figure 8 shows the rotation frequency of seven 3 μm spheres trapped in the inner ring as a function of the overall power in the higher-order BB. We repeated the experiment several times using new sets of spheres and found the rotation rates to be consistent within an error range of about 10%. As we can see from figure 8 the rotation frequency increases linearly with laser power. For linearly polarized light each photon carries $l\hbar$ of orbital angular momentum, so the angular momentum transferred to the trapped particles should be directly proportional to the laser power. As the

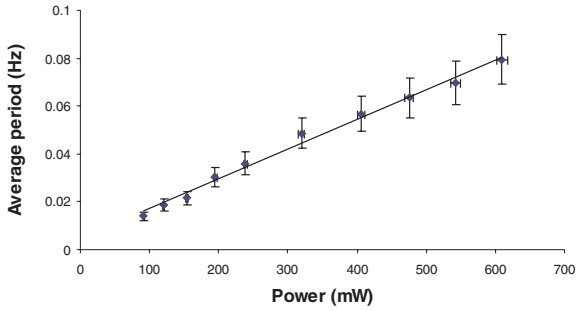

Figure 8. Average period of rotation of seven 3 μm spheres trapped on the inner ring of the high-order BB with $l = 2$ as a function of the total power of the beam.

rotation rate for a given angular momentum transfer is in first approximation determined by the Stokes drag, which is proportional to the particle speed, we expect the observed linear relationship between power and rotation rate.

We can also use the measured rotation rates to estimate the fraction of orbital angular momentum transferred to the particles. The Stokes drag for one single sphere immersed in water is

$$F = -3\pi\eta v d \tag{21}$$

where $\eta = 1 \times 10^{-3}$ Nsm^{-2} is the viscosity of water, v is the velocity of the sphere and d is the diameter of the sphere. The spheres orbit around the inner ring of the BB with a radius $r = 2.9$ μm. At a rotation rate of $\omega = 2\pi 0.08$ Hz this corresponds to a torque of $\tau_s = 1.9 \times 10^{-20}$ Nm on a single 3 μm sphere. For simplicity we estimate the total torque on the group of seven spheres to be just seven times τ_s. The total angular momentum per second for linearly polarized light is given by [7]

$$\Gamma_z = \frac{P}{2\pi\nu} l \tag{22}$$

where P is the laser power, l is the azimuthal mode index and ν is the frequency of the light ($\lambda = 1064$ nm). Assuming equal power in the rings, the measured total power of 600 mW corresponds to about $P = 15$ mW in the inner ring of the $l = 2$ BB, giving a total angular momentum flux of 1.6×10^{-17} Nm. The seven spheres cover about 90% of the inner ring area, so the total angular momentum flux of beam incident on the spheres is 1.4×10^{-17} Nm. We therefore find that we transferred about 1% of the orbital angular momentum to the spheres. This is of the same order as the expected scattering rate of light off the spheres, giving a strong indication that the mechanism for orbital angular momentum transfer in our experiment is indeed scattering.

5. Conclusions

We have calculated the total angular momentum density of BBs explicitly using the rigorous vectorial treatment. Our results have allowed us to analyse some aspects that have not been investigated, such as the AM content of azimuthally and radially polarized beams and the possibility of experimental studies of nonparaxial regimes. We have also highlighted the contrast between single- and multi-ringed paraxial beams. Furthermore, we have experimentally demonstrated for the first time the mechanical transfer of orbital angular momentum

from a high-order BB to trapped particles. The use of transparent spheres of known size made it possible to sample the angular momentum in the annular high intensity regions of the BB in a consistent and reproducible way. Quantitative studies of the rotation rates revealed that the transferred angular momentum increases linearly with laser power. The measured rotation rates correspond to a transfer of about 1% of the orbital angular momentum of the BB which is consistent with a transfer mechanism relying on scattering. Our experiment opens up the prospect of further studies examining local angular momentum density in different rings and looking at the variations predicted for circularly polarized light.

Acknowledgments

The authors would like to thank Antonia Carruthers and Svetlana Tatarkova for their help with parts of the experiment and the Engineering and Physical Science Research Council (EPSRC), the Royal Society and the Leverhulme Trust for their support. KV-S acknowledges the support of CONACYT, Mexico.

Appendix

In expression (17) the Poynting vector is calculated for nonparaxial BBs. In that case, second- and third-order terms in k_t/k_z should be considered, and the corresponding terms are given by

$$\begin{aligned}\boldsymbol{U}(\rho,\varphi,z) = {} & \frac{|E_0|^2}{2\omega\mu_0}\left(\frac{k_t}{k_z}\right)^2 \frac{l}{\rho} J_l^2[2|\alpha\sin\varphi - \beta\cos\varphi|^2\boldsymbol{u}_\varphi \\ & - (\tfrac{1}{2}(|\alpha|^2 - |\beta|^2)\sin 2\varphi - \mathrm{Re}\,(\alpha^*\beta)\cos 2\varphi)\boldsymbol{u}_\rho] \\ & + \frac{|E_0|^2 k_z}{4\omega\mu_0}\left(\frac{k_t}{k_z}\right)^3 [\{(1-\sigma)J_{l-1}J_{l-2} + (1+\sigma)J_{l+1}J_{l+2} \\ & - \sigma J_l(J_{l-1} - J_{l+1}) - [(|\alpha|^2 - |\beta|^2)\cos 2\varphi + 2\mathrm{Re}\,(\alpha^*\beta) \\ & \times \sin 2\varphi](J_{l-2}J_{l+1} + J_{l+2}J_{l-1})\}\boldsymbol{u}_\varphi + [(|\alpha|^2 - |\beta|^2)\sin 2\varphi \\ & - 2\mathrm{Re}\,(\alpha^*\beta)\cos 2\varphi](J_{l-2}J_{l+1} + J_{l+2}J_{l-1})\boldsymbol{u}_\rho]. \qquad (23)\end{aligned}$$

References

[1] Courtial J, Dholakia K, Allen L and Padgett M J 1997 Gaussian beams with very high orbital angular momentum *Opt. Commun.* **144** 210–13

[2] Allen L, Padgett M J and Babiker M 1999 The orbital angular momentum of light *Prog. Opt.* **39** 291–372

[3] Allen L, Beijersbergen M W, Spreeuw R J C and Woerdman J P 1992 Orbital angular momentum of light and the transformation of Laguerre–Gaussian laser modes *Phys. Rev.* A **45** 8185–9

[4] Durnin J, Miceli J J and Eberly J H 1987 Diffraction–free beams *Phys. Rev. Lett.* **58** 1499–501

[5] Chávez-Cerda S 1999 A new approach to Bessel beams *J. Mod. Opt.* **46** 923–30

[6] Arlt J, Hitomi T and Dholakia K 2000 Atom guiding along Laguerre–Gaussian and Bessel light beams *Appl. Phys.* B **71** 549–54

[7] Barnett S M and Allen L 1994 Orbital angular momentum and nonparaxial light-beams *Opt. Commun.* **110** 670–8

[8] He H, Friese M E J, Heckenberg N R and Rubinsztein-Dunlop H 1995 Direct observation of transfer of angular momentum to absorptive particles from a laser beam with a phase singularity *Phys. Rev. Lett.* **75** 826–9

[9] O'Neil A T and Padgett M J 2000 Three-dimensional optical confinement of micron-sized metal particles and the decoupling of the spin and orbital angular momentum within an optical spanner *Opt. Commun.* **185** 139–43

[10] Tabosa J W R and Petrov D V 1999 Optical pumping of orbital angular momentum of light in cold cesium atoms *Phys. Rev. Lett.* **83** 4967–70

[11] Friese M E J, Enger J, Rubinsztein-Dunlop H and Heckenberg N R 1996 Optical angular-momentum transfer to trapped absorbing particles *Phys. Rev.* A **54** 1593–6

[12] Simpson N B, Dholakia K, Allen L and Padgett M J 1997 Mechanical equivalence of spin and orbital angular momentum of light: an optical spanner *Opt. Lett.* **22** 52–4

[13] Allen L and Padgett M J 2000 The Poynting vector in Laguerre–Gaussian beams and the interpretation of their angular momentum density *Opt. Commun.* **184** 67–71

[14] Lax M, Louisell W H and McKnight W B 1975 *Phys. Rev.* A **11** 1365

[15] Stratton J A 1941 *Electromagnetic Theory* (New York: McGraw-Hill)

[16] Jackson J D 1962 *Classical Electrodynamics* (New York: Wiley)

[17] Padgett M J and Allen L 1995 The Poynting vector in Laguerre–Gaussian laser modes *Opt. Commun.* **121** 36–40

[18] Turunen J and Friberg A T 1993 Electromagnetic theory of reflaxicon fields *Pure Appl. Opt.* **2** 539–47

[19] Arlt J, Garcés-Chávez V, Sibbett W and Dholakia K 2001 Optical micromanipulation using a Bessel light beam *Opt. Commun.* **197** 239–45

[20] He H, Heckenberg N R and Rubinsztein-Dunlop H 1995 Optical particle trapping with higher-order doughnut beams produced using high efficiency computer generated holograms *J. Mod. Opt.* **42** 217–23

[21] Arlt J and Dholakia K 2000 Generation of high-order Bessel beams by use of an axicon *Opt. Commun.* **177** 297–301

[22] Arlt J, Dholakia K, Soneson J and Wright E M 2001 Optical dipole traps and atomic waveguides based on Bessel light beams *Phys. Rev.* A **63** 063602

[23] Ashkin A, Dziedzic J, Bjorkholm J and Chu S 1986 Observation of a single-beam gradient force optical trap for dielectric particles *Opt. Lett.* **11** 288–90

[24] O'Neil A T, MacVicar I, Allen L and Padgett M J 2002 The intrinsic and extrinsic nature of the orbital angular momentum of a light beam *Phys. Rev. Lett.* **88** 053601

[25] Arlt J Unpublished